

## Article

# Treatment of Phenol-Containing Coal Chemical Biochemical Tailwater by Catalytic Ozonation Using Mn-Ce/ $\gamma$ -Al<sub>2</sub>O<sub>3</sub>

Jun Zhou , Yongjun Sun , Wenquan Sun and Fei Hong

College of Urban Construction, Nanjing Tech University, Nanjing 211816, China

\* Correspondence: zhoujun0913@126.com

**Abstract:** In this study, a Mn-Ce/ $\gamma$ -Al<sub>2</sub>O<sub>3</sub> catalyst with multiple active components was prepared through the doping–calcination method for advanced treatment of coal chemical biochemical treatment effluent and characterized by X-ray diffraction, X-ray fluorescence spectroscopy, scanning electron microscopy, and BET analysis. In addition, preparation and catalytic ozonation conditions were optimized, and the mechanism of catalytic ozonation was discussed. The Mn-Ce/ $\gamma$ -Al<sub>2</sub>O<sub>3</sub> catalyst significantly enhanced COD and total phenol removal in reaction with ozone. The characterization results suggested that the pore structure of the optimized Mn-Ce/ $\gamma$ -Al<sub>2</sub>O<sub>3</sub> catalyst was significantly improved. After calcination, the metallic elements Mn and Ce existed in the form of the oxides MnO<sub>2</sub> and CeO<sub>2</sub>. The best operating conditions in the study were as follows: (1) reaction time of 30 min, (2) initial pH of 9, (3) ozone dosage of 3.0 g/h, and (4) catalyst dosage of 30 g/L. The removal efficiency of COD and total phenol from coal chemical biochemical tail water was reduced with the addition of tert-butanol, which proves that hydroxyl radicals ( $\bullet$ OH) played a leading role in the Mn-Ce/ $\gamma$ -Al<sub>2</sub>O<sub>3</sub> catalytic ozonation treatment process of biochemical tailwater. Ultraviolet absorption spectroscopy analysis indicated that some conjugated structures and benzene ring structures of organics in coal chemical biochemical tail water were destroyed. This work proposes the utilization of the easily available Mn-Ce/ $\gamma$ -Al<sub>2</sub>O<sub>3</sub> catalyst and exhibits application prospects for the advanced treatment of coal chemical biochemical tailwater.



**Citation:** Zhou, J.; Sun, Y.; Sun, W.; Hong, F. Treatment of Phenol-Containing Coal Chemical Biochemical Tailwater by Catalytic Ozonation Using Mn-Ce/ $\gamma$ -Al<sub>2</sub>O<sub>3</sub>. *Catalysts* **2022**, *12*, 1019. <https://doi.org/10.3390/catal12091019>

Academic Editors: Oh Wen Da, Yueping Bao and Chong Wang

Received: 8 August 2022

Accepted: 5 September 2022

Published: 8 September 2022

**Publisher's Note:** MDPI stays neutral with regard to jurisdictional claims in published maps and institutional affiliations.



**Copyright:** © 2022 by the authors. Licensee MDPI, Basel, Switzerland. This article is an open access article distributed under the terms and conditions of the Creative Commons Attribution (CC BY) license (<https://creativecommons.org/licenses/by/4.0/>).

**Keywords:** catalyst; catalytic ozonation; activated alumina; biochemical tail water; advanced treatment

## 1. Introduction

Industrial phenol-containing wastewater has become a common type of wastewater in industrial production due to its wide range of sources and strong hazards. Its main sources are chemical industries such as petroleum, gas, coking and oil refining, and industries that use phenol and its derivatives as raw materials or products [1]. Phenolic compounds are a class of polar, weakly acidic and ionizable organic compounds that are toxic and difficult to degrade. Phenolic compounds are protoplasmic poisons that are toxic to all organisms, causing the coagulation and denaturation of proteins. If phenol-containing wastewater is directly discharged, it causes great harm to aquatic environments [2]. Due to the biologically toxic and stable structures of most of the phenolic substances, conventional biological treatment is insufficient to achieve compliance with wastewater treatment [3]. Therefore, the technology of in-depth and efficient treatment of phenol-containing wastewater has become an urgent problem to be solved.

At present, treatment methods can be roughly divided into three categories: physical methods [4], chemical methods [5–7] and biological methods [8]. The physical treatment of wastewater is simple and highly efficient, with strong operability and demonstrating obvious treatment effects with high costs. The biological treatment method involves decomposing pollutants in wastewater by domesticating the metabolic activities of microorganisms to achieve the effect of purifying sewage. The biological method has high requirements on the biodegradability of the influent water. Coal chemical biochemical tailwater mostly contains refractory phenolic substances and has poor biodegradability [9].

Phenolic substances in coal chemical biochemical tailwater have toxic effects on microorganisms [3]. Chemical treatment methods have fast reaction rates and high processing efficiency. Some of the most widely used chemical treatment methods are the advanced oxidation processes (AOPs). AOPs use free radicals with high redox potential to degrade refractory and hazardous organic contaminants in wastewater [10,11]. Among them, the Fenton process has been widely used and is considered one of the most effective methods to treat phenol-containing wastewater [12]. In this process,  $H_2O_2$  is activated to form hydroxyl radicals in the presence of  $Fe^{2+}$ . The hydroxyl radicals oxidize organic compounds in wastewater, and  $Fe(OH)_3$  produced at the same time can also play a role in coagulation to further remove organic pollutants [13]. Fenton process has strict requirements on the pH of the reaction system and will generate a large amount of iron sludge [14]. Therefore, some improved processes that combine the traditional Fenton process with physicochemical technologies, such as light and electricity, have been researched to reduce the generation of secondary pollution. However, the photoelectric-Fenton process has higher energy consumption and costs [15]. Among AOPs, ozonation has attracted much attention attributable to its high oxidization capability, quick reaction speed, versatile operation, and lack of secondary pollutants [16,17]. However, limited oxidation capacity and selective oxidation of molecular ozone cause unsatisfying degradation of some pollutants [18,19]. In order to solve the problems of ozonation, catalytic ozonation is favored by researchers due to its high catalytic activity, reusable catalyst, and lack of a need for the addition of other chemicals and energy [11]. To date, several types of heterogeneous catalysts have been used to catalyze ozonation, such as iron oxides/hydroxyl oxides, bimetallic/polymetallic oxides, carbon-based materials, and metal/metal oxides supported on the carrier.

In recent years,  $Al_2O_3$  has been widely used as a catalyst support due to its low cost, high surface area, mesoporosity, high stability and many Lewis acid sites, which are conducive to the adsorption of organic substances. The surface of  $Al_2O_3$  is rich in hydroxyl groups ( $-OH$ ), which can effectively promote the generation of hydroxyl radicals [20,21]. Considering that manganese oxides have the advantages of high redox potential, environmental friendliness, low cost, and low water solubility, manganese oxides are selected as active components supported on the catalyst for catalytic ozonation [22,23].  $MnO_2$  nanoparticles supported on the activated carbon also exhibited high catalytic activity to remove Congo red dye [24]. Long-term disposal of the manganese catalyst in wastewater will lead to the dissolution of the active components, resulting in secondary pollution and reducing the lifetime of the catalyst. Cerium oxides are commonly used catalysts with excellent redox properties and good oxygen storage capacity [25,26]. The addition of the element Ce can generate more surface vacancies, improve the activity of the catalyst, and significantly improve the stability of the catalyst [27]. Cerium oxides can accelerate the activation of lattice oxygen, make the dispersion of active components in the catalyst higher, and their combination with other active metals can also produce synergistic effects. At the same time, it will also improve the anti-poisoning ability and stability of the catalyst, resulting in a longer service life of the catalyst. Therefore, to degrade phenol-containing tailwater after secondary biochemical treatment, activated alumina was selected as the catalyst carrier, and Mn and Ce metal active components were supported on the carrier to synthesize a heterogeneous catalyst for catalytic ozonation.

In this study, activated alumina loaded with Mn and Ce was prepared via a doping-calcination method as a high-efficiency heterogeneous catalyst,  $Mn-Ce/\gamma-Al_2O_3$ , for catalytic ozonation. The catalyst was applied to the research of advanced treatment of phenol-containing coal chemical biochemical tailwater. The application of X-ray diffraction (XRD), X-ray fluorescence spectroscopy (XRF), and scanning electron microscopy (SEM) were used to analyze the characteristics of  $Mn-Ce/\gamma-Al_2O_3$  catalysts. To optimize the performance of the catalytic ozonation system, the effects of  $Mn-Ce/\gamma-Al_2O_3$  catalyst dosage, ozone dosage, reaction time, initial pH, and other factors were studied. The stability of the  $Mn-Ce/\gamma-Al_2O_3$  catalyst was researched. The heterogeneous catalytic ozonation reaction

mechanism of the Mn-Ce/ $\gamma$ -Al<sub>2</sub>O<sub>3</sub> catalyst was explored by radical quencher and UV absorption spectroscopy.

## 2. Results and Discussion

### 2.1. Effect of Preparation Conditions of Mn-Ce/ $\gamma$ -Al<sub>2</sub>O<sub>3</sub> Catalyst on Pollutant Removal

The water quality parameters of the wastewater used in this paper are shown in Table 1. As shown in Figure 1a,b, with the increase in the ratio of Mn and Ce, the degradation of total phenol (meaning the total amount of phenol in wastewater) and chemical oxygen demand (COD) in wastewater showed a trend of first rising and then decreasing. As the ratio of Mn and Ce increases from 1:3 to 1:2, the degradation effect of the catalytic ozonation system is obviously improved. When Mn: Ce = 1:1, the catalytic ozonation degradation effect is the best, and the removal efficiencies of total phenol and COD are 40.32% and 67.71%, respectively. Insufficient active components may cause a lack of active sites, but in excess, catalytic activity decreases due to clusters of active components formed on the catalyst surface [28]. Figure 1c,d shows that when the calcination temperature is 400–900 °C, with the increase in calcination temperature, the effect of catalytic ozonation degradation of wastewater showed a trend of increasing first and then decreasing. The removal efficiency of total phenol and COD in wastewater reached maximum values of 42.56% and 68.98%, respectively, when the calcination temperature was 500 °C. When the calcination temperature was too low, the boehmite and active components in the  $\gamma$ -Al<sub>2</sub>O<sub>3</sub> carrier did not completely decompose, resulting in a low catalytic effect. With the increase in calcination temperature, the pore structure of the catalyst is gradually formed, and the metal salt is continuously converted to metal oxide and dispersed on the surface of the catalyst. The active sites are gradually increased, resulting in enhanced catalytic activity. However, with the further increase of the calcination temperature, the metal oxide may melt, the pores may be blocked, and the catalyst may be sintered, resulting in the reduction of effective active sites, and the catalytic activity of the catalyst may be greatly reduced [29]. As shown in Figure 1e,f, when the roasting time was 1 h, the removal efficiencies of total phenol and COD were 34.65% and 51.78%, respectively. The removal efficiency of total phenol and COD reached maximum values of 44.23% and 72.65% with a roasting time of 3 h. Metal could not be completely oxidized to generate highly active components through a shorter calcination time. Metal oxides would sinter together, resulting in a lower specific surface area and the dispersion of metal oxides with too long a roasting time [30].

**Table 1.** Water quality analysis of coal chemical biochemical tailwater.

Index	Unit	Method	Content
COD	mg/L	Potassium dichromate method [31]	219.1
NH <sub>3</sub> -N	mg/L	Nessler's reagent colorimetry [31]	12.6
pH	/	pH meter	7.05
Conductivity	$\mu$ s/cm	Conductivity meter	2.6
Turbidity	NTU	Turbidimeter	68
Chroma	PCU	Colorimeter	1780
Total phenols	mg/L	4-Aminoantipyrine Spectrophotometry [32]	36.52

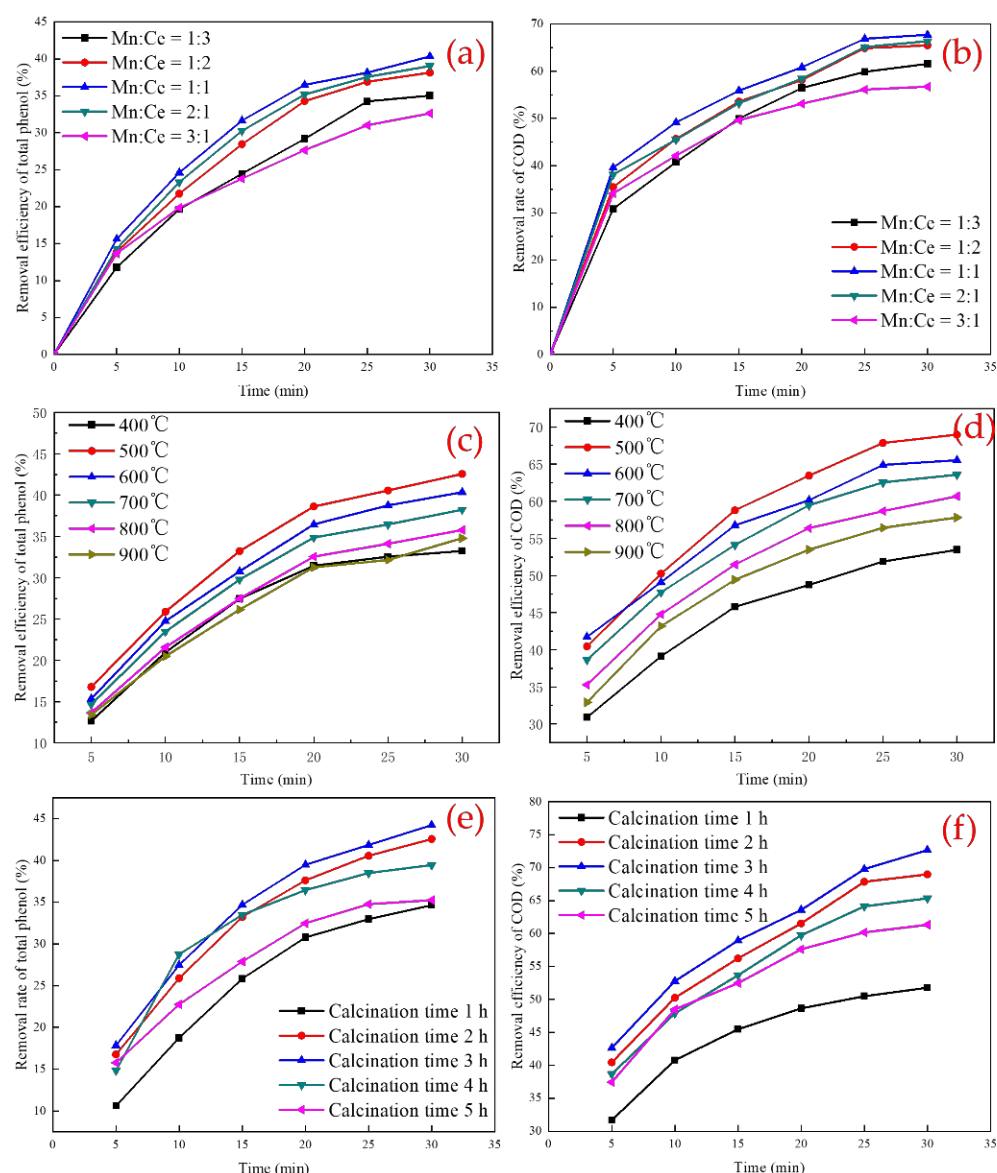


**Figure 1.** Effect of different preparation conditions on total phenol and COD removal efficiencies: (a) effect of Mn:Ce doping ratio on total phenol removal efficiency; (b) effect of Mn:Ce doping ratio on COD removal efficiency; (c) effect of calcination temperature on total phenol removal efficiency; (d) effect of calcination temperature on COD removal efficiency; (e) effect of calcination time on total phenol removal efficiency; (f) effect of calcination time on COD removal efficiency.

## 2.2. Characterization of the Mn-Ce/ $\gamma$ -Al<sub>2</sub>O<sub>3</sub> Catalyst

### 2.2.1. SEM Characterization

Figure 2 shows that the surface of blank alumina has a certain degree of roughness, irregular shape, and many depressions and pores, providing more points for the loaded metal. When the calcination temperature rises from 400 °C to 500 °C, it can be seen that the particle distribution of the carrier is more uniform, the pore structure is more abundant, and there are more fold structures. Increasing the calcination temperature properly can increase the surface roughness, which is conducive to the adhesion of manganese dioxide and cerium oxide [33]. When the temperature rises from 500 °C to 900 °C, an obvious molten layer appears on the surface of the catalyst; the surface becomes relatively smooth, the pore structure disappears, the specific surface area of the catalyst decreases and the oxides melt each other. With the increase in temperature, the small crystals dispersed on the surface of the catalyst gradually increase, showing irregular polyhedrons [34]. The

size of the alumina matrix gradually decreases, making the active site distribution more dispersed. However, when the temperature is too high, it can be seen from the above figure that the roughness of the catalyst surface decreases, resulting in the mutual connection of crystals and the change of the concave-convex characteristics of the carrier surface, the destruction of the pore structure and the reduction of the number of active sites.

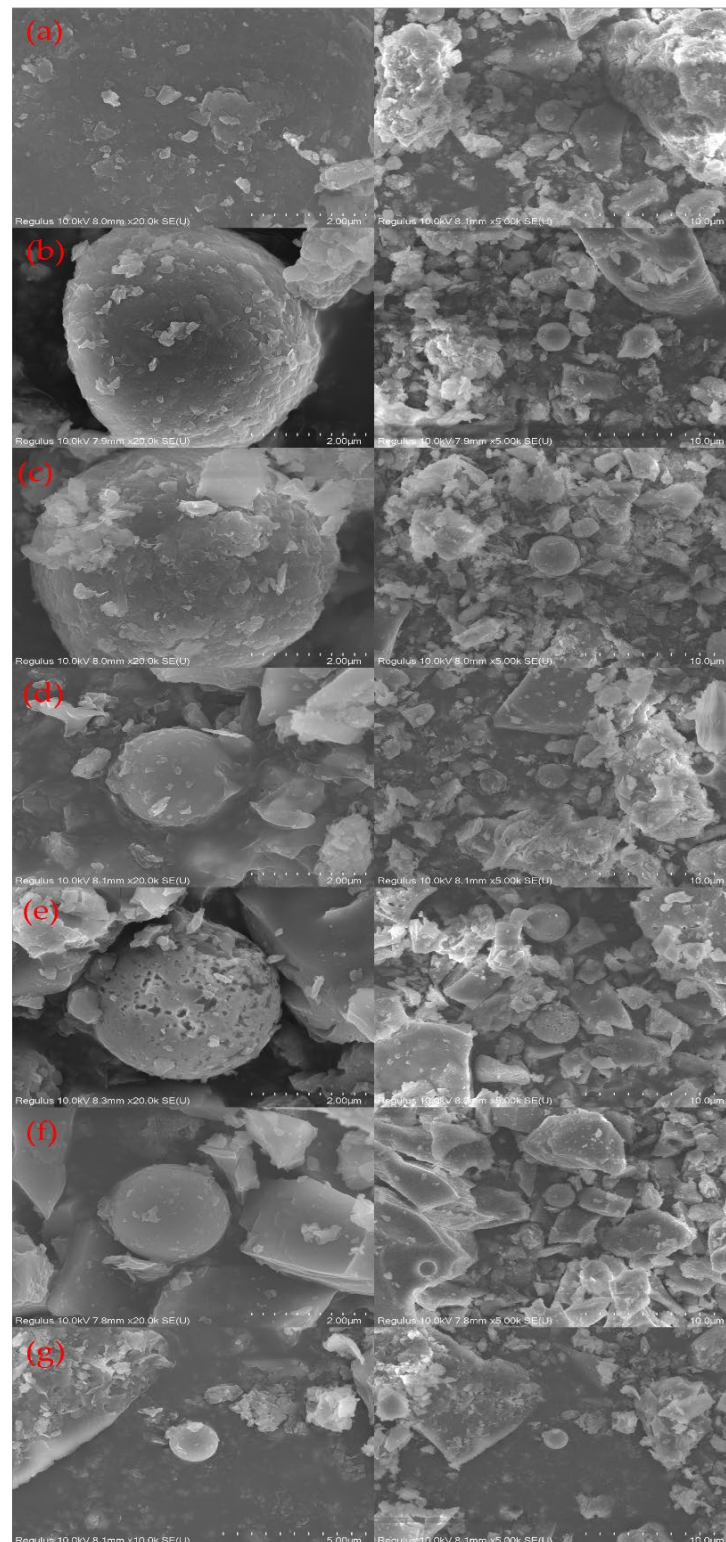


**Figure 2.** SEM characterization of catalysts: (a)  $\gamma$ -Al<sub>2</sub>O<sub>3</sub> sample; (b) 400 °C, (c) 500 °C, (d) 600 °C, (e) 700 °C, (f) 800 °C, (g) 900 °C.

### 2.2.2. XRD Characterization

As presented in Figure 3, the diffraction peak spectrum of the blank sample shows that the characteristic diffraction peak of  $\text{Al}_2\text{O}_3$  was found at  $35.2^\circ$  and  $67.9^\circ$ , and the characteristic diffraction peak of  $\text{CeO}_2$  is found at the diffraction angles of  $28.5^\circ$ ,  $33.1^\circ$ ,  $47.5^\circ$  and  $56.4^\circ$  (JCPDS#43-1002) [35]. Compared with the blank sample, the diffraction peak of  $\text{CeO}_2$  has higher intensity, which illustrates that the metal element Ce was successfully supported on the catalyst. The obvious diffraction peaks at  $2\theta = 12.7^\circ$ ,  $18.1^\circ$ ,  $28.8^\circ$ ,  $37.5^\circ$  and  $41.2^\circ$  are consistent with  $\text{MnO}_2$  (JCPDS#44-0141), indicating that the metal element Mn in the catalyst is mainly in the form of  $\text{MnO}_2$ . The observation of  $\text{CeO}_2$  and  $\text{MnO}_2$  might be the reason for the high COD and total phenol removal efficiency by Mn-Ce/ $\gamma$ - $\text{Al}_2\text{O}_3$  catalytic ozonation in Figure 1. Compared with Mn-Ce/ $\gamma$ - $\text{Al}_2\text{O}_3$  catalyst before use, the intensity of characteristic diffraction peaks of  $\text{MnO}_2$  and  $\text{CeO}_2$  in catalyst after repeated use decreased, suggesting the reduction of crystal forms  $\text{MnO}_2$  and  $\text{CeO}_2$ . This may be the result of the loss of active components Mn and Ce in the Mn-Ce/ $\gamma$ - $\text{Al}_2\text{O}_3$  catalyst after repeated use. Combined with the result of XRF, the loss of active components in the Mn-Ce/ $\gamma$ - $\text{Al}_2\text{O}_3$  catalyst is small after repeated use. The stability of the catalyst is excellent.

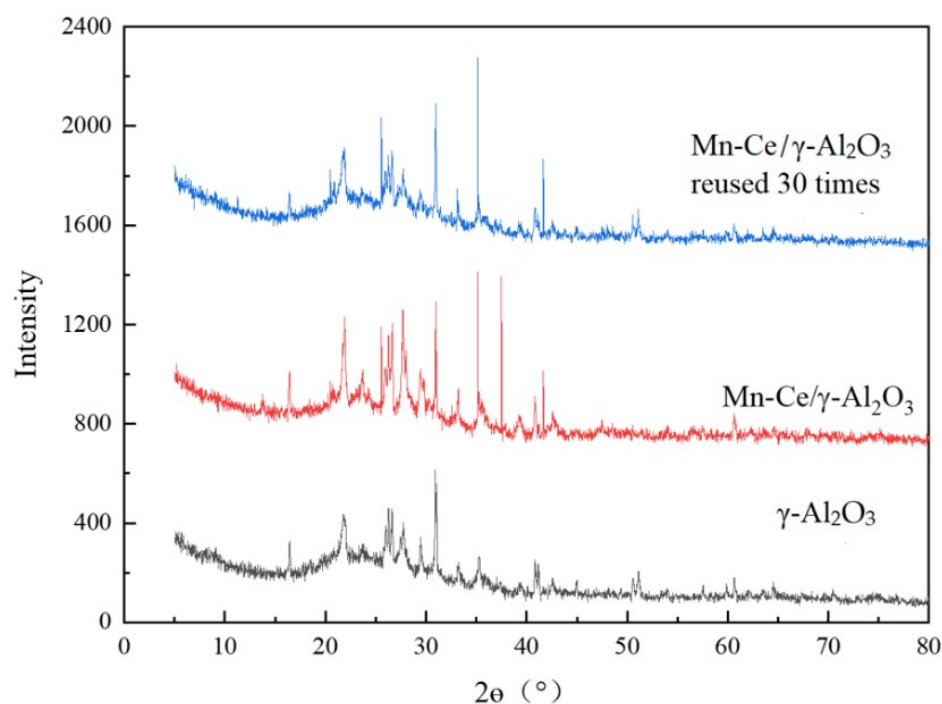


Figure 3. XRD characterization of Mn-Ce/ $\gamma$ - $\text{Al}_2\text{O}_3$  catalysts.

### 2.2.3. XRF Characterization

The XRF results are shown in Table 2. The main elements contained in the blank carrier are Na, Al, Si and Ca, mainly in the form of  $\text{Na}_2\text{O}$ ,  $\text{Al}_2\text{O}_3$ ,  $\text{SiO}_2$  and  $\text{CaO}$ . The active metal elements Mn and Ce in the Mn-Ce/ $\gamma$ - $\text{Al}_2\text{O}_3$  catalyst are in the form of  $\text{MnO}_2$  and  $\text{CeO}_2$ , with the contents of 2.832% and 0.875%, respectively, while the contents of  $\text{MnO}_2$  and  $\text{CeO}_2$  in the blank sample are only 0.174% and 0.085%. This indicates that the metal elements Mn and Ce were successfully supported on the catalyst. As the utilization time of the catalyst increased, a small loss of active components on the surface and inside the catalyst was found [36]. The contents of  $\text{MnO}_2$  and  $\text{CeO}_2$  are reduced by 0.368% and 0.104%, indicating that the preparation method of catalysts was valid and the prepared Mn-Ce/ $\gamma$ - $\text{Al}_2\text{O}_3$  catalyst had good stability. Compared with the catalyst that was recycled 30 times, the loss of supported elements is small, and there is basically no secondary pollution.

**Table 2.** XRF characterization of Mn-Ce/ $\gamma$ -Al<sub>2</sub>O<sub>3</sub> catalyst (wt, %).

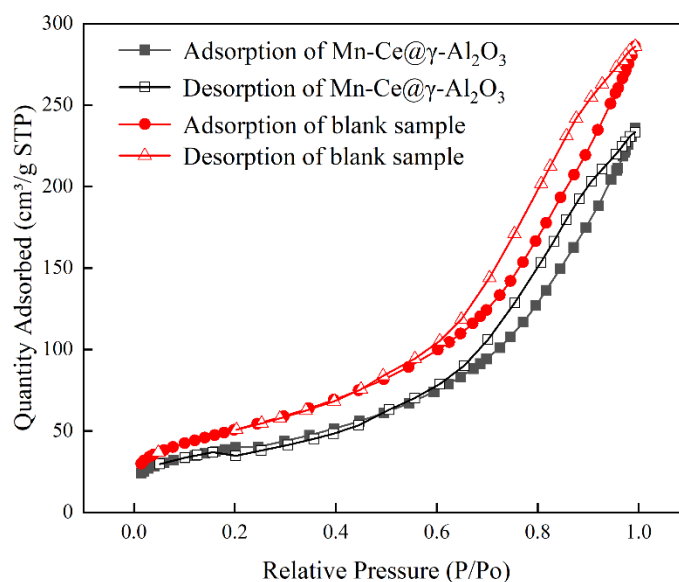
Materials	Na <sub>2</sub> O	MgO	Al <sub>2</sub> O <sub>3</sub>	SiO <sub>2</sub>	K <sub>2</sub> O	CaO	MnO <sub>2</sub>	CeO <sub>2</sub>
Blank sample	6.581	2.93	18.77	60.384	1.66	6.24	0.174	0.085
Mn-Ce/ $\gamma$ -Al <sub>2</sub> O <sub>3</sub>	5.476	2.609	17.92	59.327	1.6	5.644	2.832	0.875
Mn-Ce/ $\gamma$ -Al <sub>2</sub> O <sub>3</sub> after utilization 10 times	6.817	2.564	17.932	58.612	1.63	5.522	2.652	0.866
Mn-Ce/ $\gamma$ -Al <sub>2</sub> O <sub>3</sub> after utilization 20 times	3.7	2.657	18.613	60.794	1.586	5.242	2.555	0.803
Mn-Ce/ $\gamma$ -Al <sub>2</sub> O <sub>3</sub> after utilization 30 times	5.376	2.569	18.151	61.234	1.706	5.24	2.464	0.771

#### 2.2.4. BET Analysis

BET analysis was performed to investigate the specific surface area, pore volume, pore size, and adsorption characteristics of the catalysts. The specific surface area, pore volume and pore size are shown in Table 3. Metal oxide loading on  $\gamma$ -Al<sub>2</sub>O<sub>3</sub> increased the specific surface area and pore volume but decreased the pore size. The increase in the specific surface area was observed due to the addition of a pore-forming agent. The addition of a pore-forming agent resulted in a larger specific surface area and pore volume. Figure 4 presents the N<sub>2</sub> adsorption–desorption isotherms of the samples. Both the blank sample and the Mn-Ce/ $\gamma$ -Al<sub>2</sub>O<sub>3</sub> catalyst showed typical type IV isotherms and H3 hysteresis loops, indicating that a mesoporous structure existed in the Mn-Ce/ $\gamma$ -Al<sub>2</sub>O<sub>3</sub> catalyst and the internal structure was a slit-like pore structure. The mesoporous structure contributed to the mass transfer and adsorption of pollutants [37].

**Table 3.** BET characterization analysis of Mn-Ce/ $\gamma$ -Al<sub>2</sub>O<sub>3</sub> catalyst.

Sample	Specific Surface Area (m <sup>2</sup> /g)	Average Pore Volume (cm <sup>3</sup> /g)	Average Pore Size (nm)
$\gamma$ -Al <sub>2</sub> O <sub>3</sub>	153.46	0.37	9.65
Mn-Ce/ $\gamma$ -Al <sub>2</sub> O <sub>3</sub>	195.93	0.48	8.61

**Figure 4.** Adsorption and desorption curves of catalysts.

#### 2.3. Stability and Sustainability of Mn-Ce/ $\gamma$ -Al<sub>2</sub>O<sub>3</sub> Catalyst

In order to investigate the stability of the catalyst, the catalyst was repeatedly used 30 times with a pH of 7, catalyst dosage of 30 g/L and ozone dosage of 2.5 g/h. Figure 5 presents that the degradation performance of biochemical tailwater gradually decreased. This phenomenon is consistent with XRD results, where the intensity of characteristic diffraction peaks of MnO<sub>2</sub> and CeO<sub>2</sub> decreased after repeated use. After the catalyst is repeatedly used 5 times, the degradation effect on wastewater begins to decrease slowly.

The degradation of organic pollutants in tailwater remained relatively high, and the removal efficiencies of total phenol and COD only decreased by 9.30% and 12.90%, respectively, when Mn-Ce/ $\gamma$ -Al<sub>2</sub>O<sub>3</sub> catalyst was repeatedly used 30 times. These results indicated that the Mn-Ce/ $\gamma$ -Al<sub>2</sub>O<sub>3</sub> catalyst was stable and could be repeatedly used.

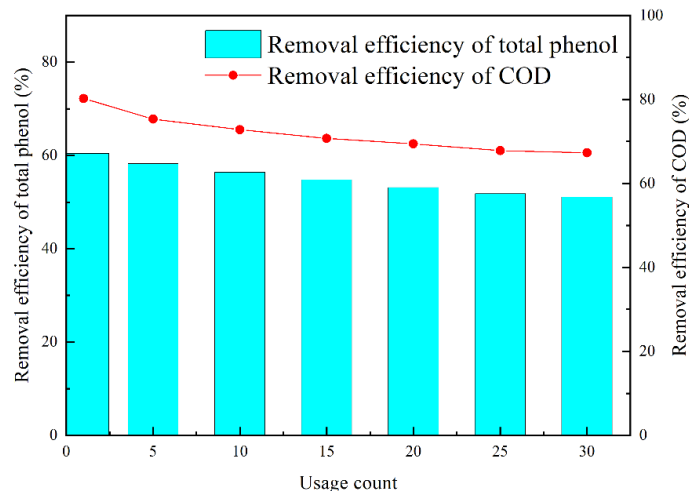


**Figure 5.** Degradation efficiency of continuous use of catalyst with pH of 7.05, catalyst dosage of 30 g/L and ozone dosage of 2.5 g/h.

## 2.4. Degradation of Coal Chemical Biochemical Tailwater by Mn-Ce/ $\gamma$ -Al<sub>2</sub>O<sub>3</sub> Catalytic Ozonation

### 2.4.1. Effects of Catalyst Dosage on Catalytic Performance

Figure 6 presents the influence of catalyst dosages on COD and total phenol removal with a pH of 7.05 and ozone dosage of 2.5 g/h. When catalyst dosages were 10–30 g/L, with the increase in dosage, COD and total phenol removal efficiencies increased rapidly. The removal efficiency of total phenol and COD increased to 58.32% and 78.91% with 30 g/L catalyst addition. However, COD and total phenol removal declined as catalyst dosage increased from 30 to 50 mg/L.

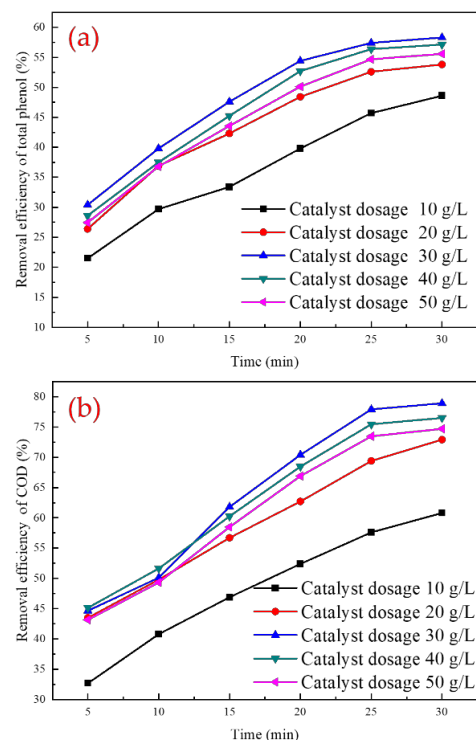


**Figure 6.** Effects of catalyst dosages on removal efficiency of (a) total phenol, (b) COD.

This is because increasing the dosage of Mn-Ce/ $\gamma$ -Al<sub>2</sub>O<sub>3</sub> catalyst increases the effective contact area of the entire reaction system and the amount of active catalytic sites, which improves the mass transfer efficiency of ozone and promotes the generation of  $\bullet$ OH, enhancing the reaction between ozone and biochemical tailwater [38]. However, when catalyst dosage exceeds a certain amount (30 g/L in this study), the effective active sites in the reaction system may reduce [39]. This will make the degradation performance worse. Meanwhile, part of the excess  $\bullet$ OH may be quenched, leading to the decline in COD and total phenol removal [40].

#### 2.4.2. Effects of Ozone Dosage on Catalytic Performance

The effect of ozone dosage on COD and total phenol removal efficiency was shown in Figure 7, with a pH of 7.05 and catalyst dosage of 30 g/L. COD and total phenol removal efficiencies increased gradually with the increase in ozone dosage. The removal efficiencies of total phenol and COD reached approximately 60.40% and 80.20%, respectively, with an ozone dosage of 3 g/h. Further increase in ozone dosage had little effect on the degradation performance of the system. The increased rate of removal efficiencies slowed down when ozone dosage reached 3 g/h. This phenomenon may be attributed to the increase in ozone dosage, causing the generation of more  $\bullet$ OH when the ozone dosage is below a certain level [41]. When the ozone in the system reaches a saturated state, the utilization rate of ozone decreases, and further increases in ozone dosage have little improvement on the degradation of wastewater [42]. On the other hand, the residue organics were structurally stable and difficult to degrade. Considering the cost and pollutants removal efficiency, 3 g/h was selected as an optimal ozone dosage.

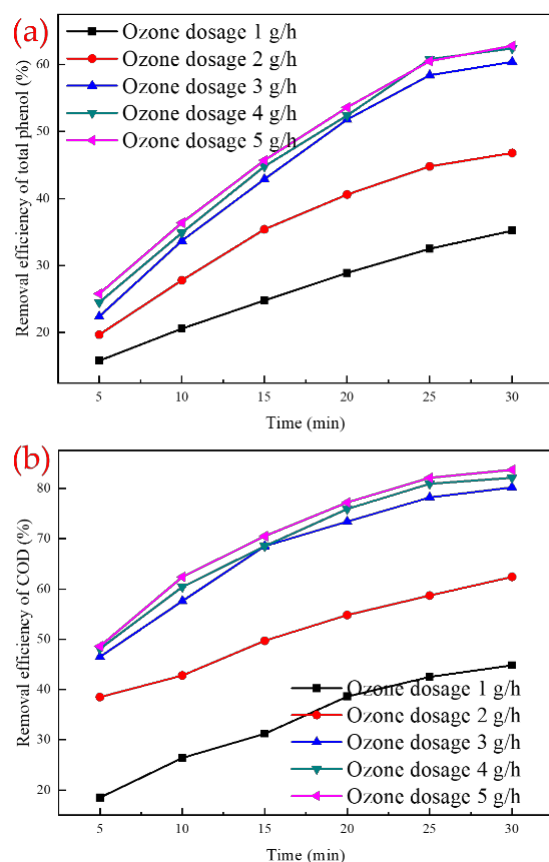


**Figure 7.** Effects of ozone dosages on removal efficiency of (a) total phenol and (b) COD.

#### 2.4.3. Effects of Reaction Time on Catalytic Performance

Figure 8 depicts that the removal efficiencies of total phenol and COD rise rapidly at the beginning of the reaction. After 20 min, total phenol and COD removal efficiencies

increase relatively slowly. Thereafter, the removal efficiencies of total phenol and COD increase insignificantly when the reaction time increases to 120 min. This is because the concentration of organic matter in the initial reaction system is relatively high, and the active oxygen-containing groups, such as hydroxyl radicals generated by the catalytic ozonation of the catalyst, can rapidly react with the pollutants to degrade the pollutants. Therefore, the removal efficiencies of total phenol and COD in the reaction system rise rapidly. As the reaction time is prolonged, the concentration of pollutants is lower, and remaining organic pollutants are difficult to degrade. Therefore, the optimal reaction time is 30 min in the experiments.

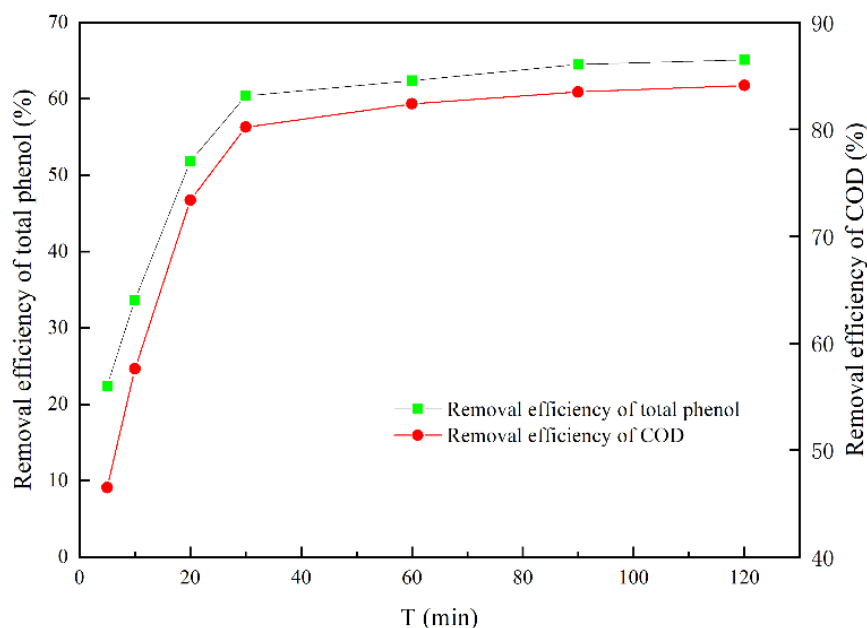


**Figure 8.** Effects of reaction time on removal efficiency of total phenol and COD.

#### 2.4.4. Effects of pH on Catalytic Performance

The pH of the solution dramatically affects the performance of the catalyst and is considered an essential parameter in wastewater treatment [43,44]. Figure 9 shows that the removal efficiency of total phenol gradually increased as the initial pH increased with a catalyst dosage of 30 g/L and an ozone dosage of 3 g/h. When the pH value rose from 5.1 to 10.05, the total phenol removal efficiency increased from 55.43% to 64.24%. Correspondingly, COD removal efficiency improved from 74.62% to 82.95%. This is because ozone molecules become the main oxidant in the reaction system under acidic conditions, and the selectivity is high, resulting in incomplete oxidation of organic matter [36]. Under alkaline conditions, the concentration of  $\text{OH}^-$  in the solution increases, and  $\text{OH}^-$ , as the initiator of the free radical reaction, can promote the adsorption and decomposition of ozone by the catalyst surface to generate more active free radicals such as  $\bullet\text{OH}$  and improve the reaction rate. The surface charge of the catalyst is also affected by the pH of the wastewater. However, when the pH continues to increase, the utilization of the initiator in the reaction system is saturated. The excess  $\text{OH}^-$  will cause the deprotonation of the hydroxyl group on the catalyst surface and change the charge of the catalyst surface, thereby weakening the free radical reaction, which reduces the degradation performance of coal chemical biochemical tailwater [45]. The initial pH of 9.08 was selected as the optimal operational pH value in the subsequent experiment.

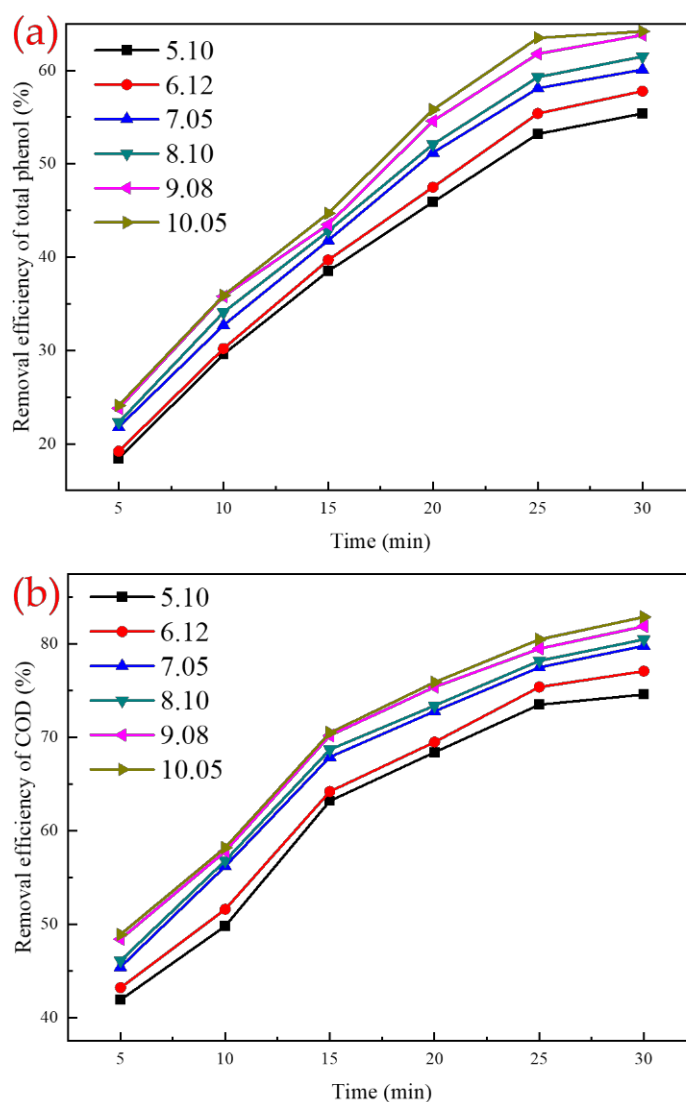


**Figure 9.** Effects of ozone pH on removal efficiency of (a) total phenol and (b) COD.

## 2.5. Ozone Catalytic Oxidation Mechanism of Mn-Ce/ $\gamma$ -Al<sub>2</sub>O<sub>3</sub> Catalyst

### 2.5.1. Effect of Free Radical Inhibitors on Catalytic Ozonation Performance

The effect of tert-butanol (TBA) on the ozone catalytic degradation system is shown in Figure 10. The addition of TBA obviously reduces the effect of catalytic ozonation on the degradation of coal chemical biochemical tailwater. After the addition of 30, 50 and 100 mg/L TBA to the catalytic ozonation system, the removal efficiency of total phenol in biochemical tailwater decreased by 11.90%, 24.62% and 32.10% after 30 min, respectively. Under the same conditions, the removal efficiency of COD in biochemical tailwater decreased by 15.00%, 27.02% and 29.80% after 30 min, respectively. TBA is a common hydroxyl radical inhibitor. It can inhibit the chain reaction of free radicals by reacting with hydroxyl radicals to form highly inert substances and inhibit the oxidation of other organic substances by hydroxyl radicals [46]. The addition of TBA reduced the degradation performance of biochemical tailwater as a result of the competition between TBA and organics in wastewater for hydroxyl radicals generated by ozone decomposition. This finding indirectly proved that the degradation of biochemical tailwater by catalytic ozonation follows a hydroxyl radical chain reaction. However, under the condition of TBA addition, the degradation performance of the catalytic ozonation system is still better than that of the ozonation system, which indicates that hydroxyl radicals are not the only oxidant in the reaction system.

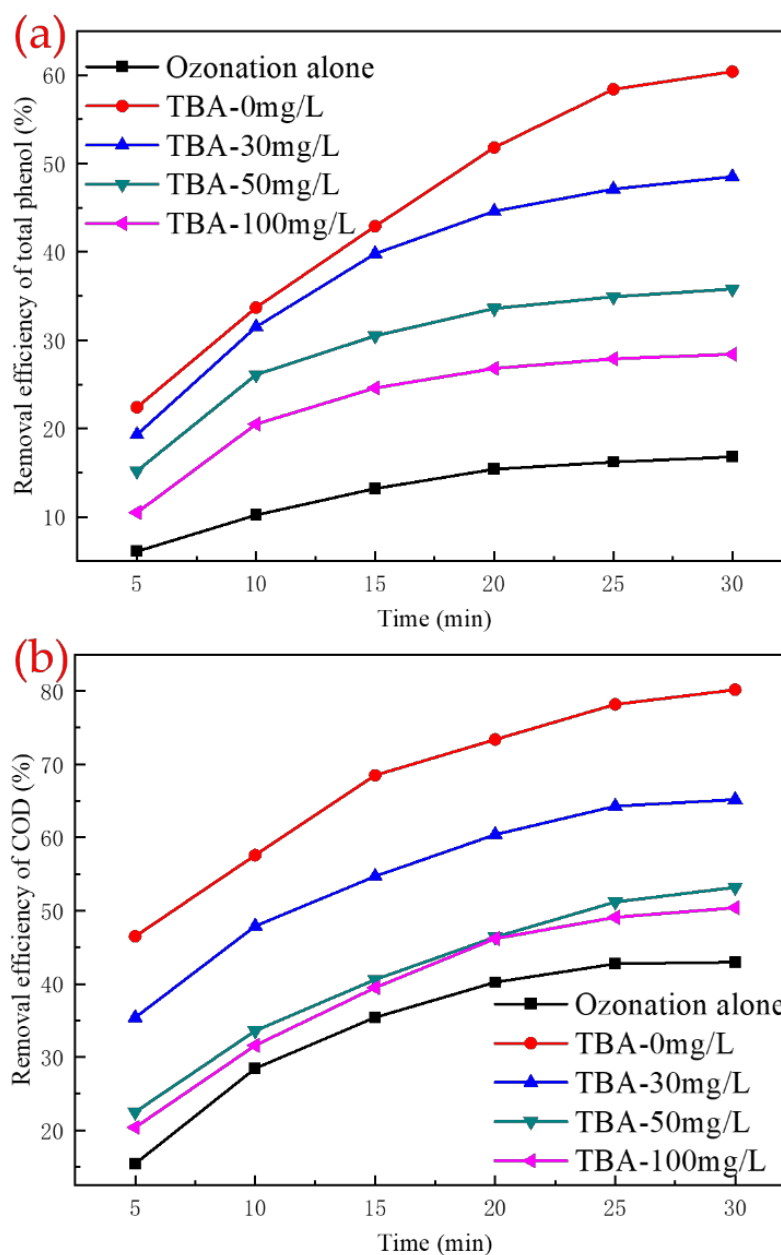


**Figure 10.** Effect of tert-butanol dosage on removal efficiency for (a) total phenol and (b) COD.

### 2.5.2. UV-Vis Absorption Peak at Different Catalytic Ozonation Times

As shown in Figure 11, the UV absorption peak of the effluent sample treated with biochemical tailwater shows a significant decrease in the range of  $\lambda = 200\text{--}500\text{ nm}$ , indicating that the conjugated structure, the auxiliary color groups and unsaturated organic matter were effectively degraded. When the reaction is carried out for 10 min, the absorption peak at 200–500 nm is significantly decreased. With the prolongation of catalytic ozonation, the intensity of the absorption peak at 200–500 nm reduced gradually. After 20 min, the UV absorbance changed slightly, indicating that most organic matter and chromophores had been degraded [47].

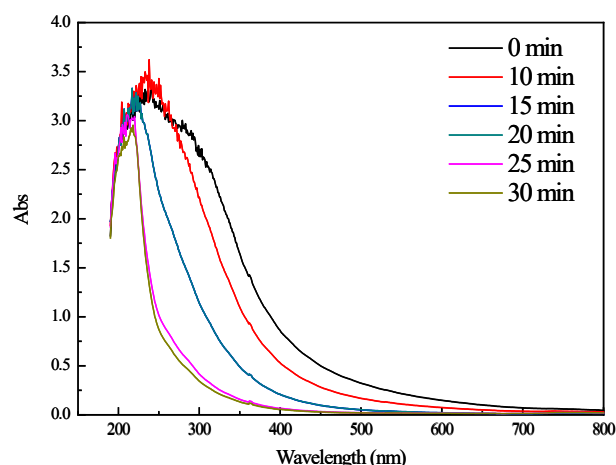


**Figure 11.** UV-Vis analysis at different catalytic ozonation times with pH of 9, initial COD of 121.5 mg/L, catalyst dosage of 30 g/L and ozone dosage of 3 g/h.

### 3. Materials and Methods

#### 3.1. Experimental Materials

Manganese nitrate, sodium silicate, sodium bicarbonate, copper nitrate trihydrate ( $\text{Cu}(\text{NO}_3)_2 \cdot 3\text{H}_2\text{O}$ ), cerium nitrate ( $\text{Ce}(\text{NO}_3)_3 \cdot 6\text{H}_2\text{O}$ ), cobalt nitrate hexahydrate ( $\text{Co}(\text{NO}_3)_2 \cdot 6\text{H}_2\text{O}$ ), ferric nitrate nonahydrate ( $\text{Fe}(\text{NO}_3)_3 \cdot 9\text{H}_2\text{O}$ ), nitric acid, sulfuric acid, bismuth nitrate, potassium bromate and sodium hydroxide were all analytical grade and purchased from Nanjing Chemical Reagent Co., Ltd (Nanjing, China). Tert-butanol ( $\text{C}_4\text{H}_{10}\text{O}$ ) was analytical grade and purchased from Sinopharm Chemical Reagent Co., Ltd (Shanghai, China). Fly ash floating beads were 100 mesh and purchased from Henan Borun Casting Material Co., Ltd (Gongyi, China). Activated alumina was 100 mesh and purchased from Nanjing Chemical Reagent Co., Ltd. Coal chemical biochemical tailwater taken from a coal chemical enterprise in Yunnan was used in the experiment. The same batch of coal chemical biochemical tailwater was used throughout the study. The water sample is dark and turbid, with a pungent odor and a little suspended matter floating on the surface. The raw water quality test results and measurement methods are shown in Table 2.

#### 3.2. Preparation of Mn-Ce/ $\gamma$ - $\text{Al}_2\text{O}_3$ Catalyst

The catalyst was prepared by a doping-calcination method [48]. A quantitative amount of nitrate solution of Mn and Ce was weighed, diluted to 100 mL in a volumetric flask, shaken evenly, and placed in a beaker as a precursor solution for later use. Next, 30 g of activated alumina and a certain amount of pore-forming agent and binder were weighed, placed in a mortar, and stirred evenly. The precursor solution and deionized water were poured into the uniformly mixed activated alumina powder, pore-forming agent, and binder. The container was shaken vigorously to make the medium uniformly mixed. The catalyst was taken out to make a spherical catalyst, and the particle size of the catalyst sphere was controlled within 4–6 mm. The catalyst was placed in an oven to dry at 105 °C for 24 h. The dried catalyst is placed in a crucible and calcined at a certain temperature in a muffle furnace. After the calcination is completed, the calcined catalyst was taken out, exposed to the air for natural cooling, and finally packaged for use.

#### 3.3. Characterization of Mn-Ce/ $\gamma$ - $\text{Al}_2\text{O}_3$ Catalysts

The surface morphology of the catalyst was characterized by SEM (ZEISS Merlin, Zeiss AG, Oberkochen, Germany). XRD (D8 Advance, Bruker, Berlin, Germany) was used to characterize the crystal morphology of transition metals in the catalyst. XRF (Axios Pw4400, PANalytical, Eindhoven, Netherlands) was used to characterize the content of metal elements and metal oxides inside the catalyst. BET analysis was used to characterize the pore

volume, pore size, and adsorption performance of the catalyst (ASAP-2020, Micromeritics Company, Norcross, GA, USA). The sample was automatically degassed at 90 °C for 1 h for the first stage and 350 °C for 4 h for the second stage, with the N<sub>2</sub> adsorption-desorption isotherm taken at 77 K.

### 3.4. Ozone Catalytic Oxidation Experiment

Figure 12 shows the schematic diagram of the catalytic reaction device used in this study. The catalytic reaction device consisted of an oxygen cylinder, an ozone generator (CF-G-3-10G, Qingdao Guolin, China), a gas flow meter, a reaction tower, and a tail gas absorption device. At the beginning of the experiment, the oxygen source was opened to pre-blow the ozone generator for 10 min, and the outlet pressure was controlled to 0.1 MPa. After the pre-blow, a quantitative amount of the prepared catalyst was added, and 400 mL of coal chemical biochemical tailwater was placed in the reaction tower. Then, the ozone generator was turned on, and the oxygen generated ozone through high-voltage discharge inside the ozone generator. By adjusting the gas flow meter of the ozone generator, we controlled the output of ozone, reserved a water outlet on the side wall of the reactor, and took samples regularly during the experiment to measure various indicators. The exhaust gas generated in the experiment was discharged after passing through the two-stage 20% KI absorption treatment device.

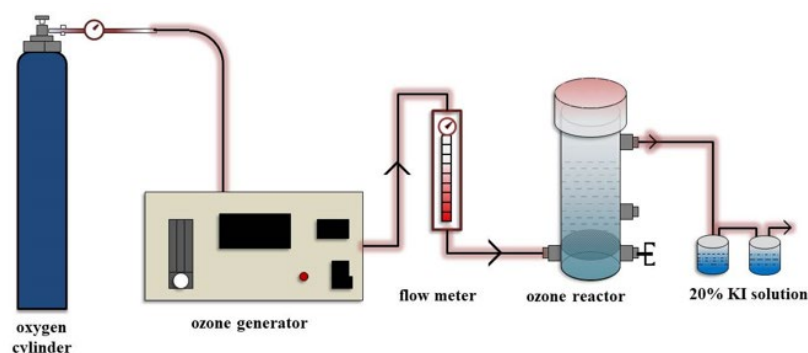


**Figure 12.** The schematic diagram of the catalytic ozone oxidation system.

The iodometric method was used to determine the gas-phase ozone concentration. The sodium indigo disulfonate method was employed to measure the ozone concentration in the liquid phase. The water samples of the outlet were tested and analyzed using UV-Vis technology (ultraviolet spectrophotometer, UV-5500, Shanghai Yuanxi Instrument Co., Ltd., Shanghai, China) with a wavelength of 190–800 nm.

## 4. Conclusions

In this study, activated alumina was used as a carrier, and Mn-Ce/ $\gamma$ -Al<sub>2</sub>O<sub>3</sub> catalyst was prepared by loading Mn and Ce by the doping-calcination method to treat coal chemical biochemical tailwater. The optimal preparation conditions of Mn-Ce/ $\gamma$ -Al<sub>2</sub>O<sub>3</sub> catalyst are presented as follows: the active metal loading ratio of Mn:Ce is 1:1, the calcination temperature is 500 °C, and the calcination time is 3.0 h. SEM analysis showed that Mn-Ce/ $\gamma$ -Al<sub>2</sub>O<sub>3</sub> catalyst had a porous structure, and more fold structures developed. Mn and Ce were successfully loaded on the surface and inside of the activated alumina in the form of MnO<sub>2</sub> and CeO<sub>2</sub>, the contents of which were 2.832 and 0.875 wt%, respectively. MnO<sub>2</sub> and CeO<sub>2</sub> might be the active components that improved the catalytic activity of Mn-Ce/ $\gamma$ -Al<sub>2</sub>O<sub>3</sub> according to the characterization analyses. The Mn-Ce/ $\gamma$ -Al<sub>2</sub>O<sub>3</sub> catalyst exhibited excellent catalytic activity on the degradation of coal chemical biochemical tailwater after repeated use. The optimal conditions for the catalytic ozonation by Mn-Ce/ $\gamma$ -Al<sub>2</sub>O<sub>3</sub> catalyst to the coal chemical biochemical tailwater were as follows: catalyst dosage 30 g/L, ozone dosage 3 g/h, initial pH 9.08, and reaction time 30 min. Alkaline conditions promoted the degradation of organic matter. The COD and total phenol removal increased to 82.95%

and 64.24%, respectively. Generation of hydroxyl radical was the dominant process in the treatment of coal chemical biochemical tailwater. This study offers a candidate catalyst for the advanced treatment of coal chemical biochemical tailwater upon catalytic ozonation. The high removal efficiency, stability and feasibility suggested the prospect of applications of catalytic ozonation for industrial wastewater.

**Author Contributions:** Conceptualization, Y.S. and W.S.; methodology, J.Z. and Y.S.; formal analysis, J.Z. and F.H.; investigation, J.Z. and F.H.; writing—original draft preparation, J.Z. and F.H.; writing—review and editing, J.Z. and Y.S.; funding acquisition, Y.S. and W.S. All authors have read and agreed to the published version of the manuscript.

**Funding:** This research received no external funding.

**Data Availability Statement:** Data are contained within the article.

**Conflicts of Interest:** The authors declare no conflict of interest.

## References

1. Venu Vinod, A.; Venkat Reddy, G. Mass transfer correlation for phenol biodegradation in a fluidized bed bioreactor. *J. Hazard. Mater.* **2006**, *136*, 727–734. [[CrossRef](#)] [[PubMed](#)]
2. Fava, F.; Armenante, P.M.; Kafkewitz, D. Aerobic degradation and dechlorination of 2-chlorophenol, 3-chlorophenol and 4-chlorophenol by a *Pseudomonas pickettii* strain. *Lett. Appl. Microbiol.* **1995**, *21*, 307–312. [[CrossRef](#)] [[PubMed](#)]
3. Zhu, H.; Ma, W.; Han, H.; Han, Y.; Ma, W. Catalytic ozonation of quinoline using nano-MgO: Efficacy, pathways, mechanisms and its application to real biologically pretreated coal gasification wastewater. *Chem. Eng. J.* **2017**, *327*, 91–99. [[CrossRef](#)]
4. Otero, M.; Zabkova, M.; Rodrigues, A.E. Comparative study of the adsorption of phenol and salicylic acid from aqueous solution onto nonionic polymeric resins. *Sep. Purif. Technol.* **2005**, *45*, 86–95. [[CrossRef](#)]
5. Huang, J.; Puyang, C.; Wang, Y.; Zhang, J.; Guo, H. Hydroxylamine activated by discharge plasma for synergetic degradation of tetracycline in water: Insight into performance and mechanism. *Sep. Purif. Technol.* **2022**, *300*, 121913. [[CrossRef](#)]
6. Huang, J.; Puyang, C.; Guo, H. Sodium percarbonate activation by plasma-generated ozone for catalytic degradation of dye wastewater: Role of active species and degradation process. *Catalysts* **2022**, *12*, 681. [[CrossRef](#)]
7. Zhang, H.; Xiao, Y.; Tian, L.; Tang, Y.; Liu, X.; Shi, Z.; Wu, Z.; Wei, Z. In-situ fabrication of a phase continuous transition Bismuth iodide/Bismuth niobate heterojunction: Interface regulation and the enhanced photodegradation mechanism. *Chem. Phys.* **2022**, *562*, 111644. [[CrossRef](#)]
8. Deng, S.; Jothinathan, L.; Cai, Q.; Li, R.; Wu, M.; Ong, S.L.; Hu, J. FeOx@GAC catalyzed microbubble ozonation coupled with biological process for industrial phenolic wastewater treatment: Catalytic performance, biological process screening and microbial characteristics. *Water Res.* **2021**, *190*, 116687. [[CrossRef](#)]
9. Awfa, D.; Ateia, M.; Fujii, M.; Johnson, M.S.; Yoshimura, C. Photodegradation of pharmaceuticals and personal care products in water treatment using carbonaceous-TiO<sub>2</sub> composites: A critical review of recent literature. *Water Res.* **2018**, *142*, 26–45. [[CrossRef](#)]
10. Yao, W.; Fu, J.; Yang, H.; Yu, G.; Wang, Y. The beneficial effect of cathodic hydrogen peroxide generation on mitigating chlorinated by-product formation during water treatment by an electro-peroxone process. *Water Res.* **2019**, *157*, 209–217. [[CrossRef](#)]
11. Yu, G.; Wang, Y.; Cao, H.; Zhao, H.; Xie, Y. Reactive oxygen species and catalytic active sites in heterogeneous catalytic ozonation for water purification. *Environ. Sci. Technol.* **2020**, *54*, 5931–5946. [[CrossRef](#)] [[PubMed](#)]
12. Hermosilla, D.; Cortijo, M.; Huang, C.P. Optimizing the treatment of landfill leachate by conventional Fenton and photo-Fenton processes. *Sci. Total Environ.* **2009**, *407*, 3473–3481. [[CrossRef](#)] [[PubMed](#)]
13. Kwan, W.P.; Voelker, B.M. Decomposition of hydrogen peroxide and organic compounds in the presence of dissolved iron and ferrihydrite. *Environ. Sci. Technol.* **2002**, *36*, 1467–1476. [[CrossRef](#)] [[PubMed](#)]
14. Silveira, J.E.; Zazo, J.A.; Pliego, G.; Casas, J.A. Landfill leachate treatment by sequential combination of activated persulfate and Fenton oxidation. *Waste Manag.* **2018**, *81*, 220–225. [[CrossRef](#)] [[PubMed](#)]
15. Altin, A. An alternative type of photoelectro-Fenton process for the treatment of landfill leachate. *Sep. Purif. Technol.* **2008**, *61*, 391–397. [[CrossRef](#)]
16. Wu, M.; Kwok, Y.H.; Zhang, Y.; Szeto, W.; Huang, H.; Leung, D.Y.C. Synergetic effect of vacuum ultraviolet photolysis and ozone catalytic oxidation for toluene degradation over MnO<sub>2</sub>-rGO composite catalyst. *Chem. Eng. Sci.* **2021**, *231*, 116288. [[CrossRef](#)]
17. Miklos, D.B.; Remy, C.; Jekel, M.; Linden, K.G.; Drewes, J.E.; Hübner, U. Evaluation of advanced oxidation processes for water and wastewater treatment—A critical review. *Water Res.* **2018**, *139*, 118–131. [[CrossRef](#)]
18. Liu, J.; Ke, L.; Liu, J.; Sun, L.; Yuan, X.; Li, Y.; Xia, D. Enhanced catalytic ozonation towards oxalic acid degradation over novel copper doped manganese oxide octahedral molecular sieves nanorods. *J. Hazard. Mater.* **2019**, *371*, 42–52. [[CrossRef](#)]
19. González-Labrada, K.; Richard, R.; Andriantsiferana, C.; Valdés, H.; Jáuregui-Haza, U.J.; Manero, M. Enhancement of ciprofloxacin degradation in aqueous system by heterogeneous catalytic ozonation. *Environ. Sci. Pollut. Res.* **2020**, *27*, 1246–1255. [[CrossRef](#)]
20. Xu, Y.; Lin, Z.; Zheng, Y.; Dacquin, J.; Royer, S.; Zhang, H. Mechanism and kinetics of catalytic ozonation for elimination of organic compounds with spinel-type CuAl<sub>2</sub>O<sub>4</sub> and its precursor. *Sci. Total Environ.* **2019**, *651*, 2585–2596. [[CrossRef](#)]

21. Bing, J.; Hu, C.; Zhang, L. Enhanced mineralization of pharmaceuticals by surface oxidation over mesoporous  $\gamma$ -Ti-Al<sub>2</sub>O<sub>3</sub> suspension with ozone. *Appl. Catal. B Environ.* **2017**, *202*, 118–126. [[CrossRef](#)]
22. Xu, X.; Zhao, J.; Jiang, Y.; Tang, X.; Zhou, Z.; Zhu, Y. Promotion of catalytic ozonation of aniline with Mn-Ce-O<sub>x</sub>/ $\gamma$ -Al<sub>2</sub>O<sub>3</sub>. *Water Sci. Technol.* **2018**, *78*, 339–346. [[CrossRef](#)] [[PubMed](#)]
23. Nawaz, F.; Xie, Y.; Xiao, J.; Cao, H.; Ghazi, Z.A.; Guo, Z.; Chen, Y. The influence of the substituent on the phenol oxidation rate and reactive species in cubic MnO<sub>2</sub> catalytic ozonation. *Catal. Sci. Technol.* **2016**, *6*, 7875–7884. [[CrossRef](#)]
24. Khan, I.; Sadiq, M.; Khan, I.; Saeed, K. Manganese dioxide nanoparticles/activated carbon composite as efficient UV and visible-light photocatalyst. *Environ. Sci. Pollut. Res.* **2019**, *26*, 5140–5154. [[CrossRef](#)] [[PubMed](#)]
25. Shen, C.; Wen, X.; Fei, Z.; Liu, Z.; Mu, Q. Visible-light-driven activation of peroxydisulfate for accelerating ciprofloxacin degradation using CeO<sub>2</sub>/Co<sub>3</sub>O<sub>4</sub> p-n heterojunction photocatalysts. *Chem. Eng. J.* **2020**, *391*, 123612. [[CrossRef](#)]
26. Lan, Y.; Sohn, H.Y.; Mohassab, Y.; Liu, Q.; Xu, B. Properties of stable nonstoichiometric nanoceria produced by thermal plasma. *J. Nanopart. Res.* **2017**, *19*, 281. [[CrossRef](#)]
27. Hočevár, S.; Krašovec, U.O.; Orel, B.; Aricó, A.S.; Kim, H. CWO of phenol on two differently prepared CuO–CeO<sub>2</sub> catalysts. *Appl. Catal. B Environ.* **2000**, *28*, 113–125. [[CrossRef](#)]
28. Zhao, L.; Ma, J.; Sun, Z.; Zhai, X. Catalytic ozonation for the degradation of nitrobenzene in aqueous solution by ceramic honeycomb-supported manganese. *Appl. Catal. B Environ.* **2008**, *83*, 256–264. [[CrossRef](#)]
29. Liu, Z.; Tu, J.; Wang, Q.; Cui, Y.; Zhang, L.; Wu, X.; Zhang, B.; Ma, J. Catalytic ozonation of diethyl phthalate in aqueous solution using graphite supported zinc oxide. *Sep. Purif. Technol.* **2018**, *200*, 51–58. [[CrossRef](#)]
30. Nakhate, P.H.; Gadipelly, C.R.; Joshi, N.T.; Marathe, K.V. Engineering aspects of catalytic ozonation for purification of real textile industry wastewater at the pilot scale. *J. Ind. Eng. Chem.* **2019**, *69*, 77–89. [[CrossRef](#)]
31. Kong, X.; Garg, S.; Chen, G.; Li, W.; Wang, Y.; Wang, J.; Ma, J.; Yuan, Y.; Waite, T.D. Coal chemical industry membrane concentrates: Characterisation and treatment by ozonation and catalytic ozonation processes. *Environ. Chem.* **2022**. [[CrossRef](#)]
32. Ho, K.; Chen, Y.; Lin, B.; Lee, D. Degrading high-strength phenol using aerobic granular sludge. *Appl. Microbiol. Biotechnol.* **2010**, *85*, 2009–2015. [[CrossRef](#)]
33. Qi, F.; Xu, B.; Chen, Z.; Feng, L.; Zhang, L.; Sun, D. Catalytic ozonation of 2-isopropyl-3-methoxypyrazine in water by  $\gamma$ -AlOOH and  $\gamma$ -Al<sub>2</sub>O<sub>3</sub>: Comparison of removal efficiency and mechanism. *Chem. Eng. J.* **2013**, *219*, 527–536. [[CrossRef](#)]
34. Li, X.; Chen, W.; Tang, Y.; Li, L. Relationship between the structure of Fe-MCM-48 and its activity in catalytic ozonation for diclofenac mineralization. *Chemosphere* **2018**, *206*, 615–621. [[CrossRef](#)] [[PubMed](#)]
35. He, S.; Luan, P.; Mo, L.; Xu, J.; Li, J.; Zhu, L.; Zeng, J. Mineralization of recalcitrant organic pollutants in pulp and paper mill wastewaters through ozonation catalyzed by Cu-Ce supported on Al<sub>2</sub>O<sub>3</sub>. *Bioresources* **2018**, *13*, 3686–3703. [[CrossRef](#)]
36. Hu, E.; Wu, X.; Shang, S.; Tao, X.; Jiang, S.; Gan, L. Catalytic ozonation of simulated textile dyeing wastewater using mesoporous carbon aerogel supported copper oxide catalyst. *J. Clean. Prod.* **2016**, *112*, 4710–4718. [[CrossRef](#)]
37. Yang, Y.; Zhao, S.; Bi, F.; Chen, J.; Li, Y.; Cui, L.; Xu, J.; Zhang, X. Oxygen-vacancy-induced O<sub>2</sub> activation and electron-hole migration enhance photothermal catalytic toluene oxidation. *Cell Rep. Phys. Sci.* **2022**, *3*, 101011. [[CrossRef](#)]
38. Huang, Y.; Cui, C.; Zhang, D.; Li, L.; Pan, D. Heterogeneous catalytic ozonation of dibutyl phthalate in aqueous solution in the presence of iron-loaded activated carbon. *Chemosphere* **2015**, *119*, 295–301. [[CrossRef](#)] [[PubMed](#)]
39. Van, H.T.; Nguyen, L.H.; Hoang, T.K.; Tran, T.P.; Vo, A.T.; Pham, T.T.; Nguyen, X.C. Using FeO-constituted iron slag wastes as heterogeneous catalyst for Fenton and ozonation processes to degrade Reactive Red 24 from aqueous solution. *Sep. Purif. Technol.* **2019**, *224*, 431–442. [[CrossRef](#)]
40. Li, W.; Qiang, Z.; Zhang, T.; Cao, F. Kinetics and mechanism of pyruvic acid degradation by ozone in the presence of PdO/CeO<sub>2</sub>. *Appl. Catal. B Environ.* **2012**, *113*, 290–295. [[CrossRef](#)]
41. Qi, F.; Chen, Z.; Xu, B.; Shen, J.; Ma, J.; Joll, C.; Heitz, A. Influence of surface texture and acid–base properties on ozone decomposition catalyzed by aluminum (hydroxyl) oxides. *Appl. Catal. B Environ.* **2008**, *84*, 684–690. [[CrossRef](#)]
42. Tan, X.; Wan, Y.; Huang, Y.; He, C.; Zhang, Z.; He, Z.; Hu, L.; Zeng, J.; Shu, D. Three-dimensional MnO<sub>2</sub> porous hollow microspheres for enhanced activity as ozonation catalysts in degradation of bisphenol A. *J. Hazard. Mater.* **2017**, *321*, 162–172. [[CrossRef](#)]
43. Khan, I.; Saeed, K.; Ali, N.; Khan, I.; Zhang, B.; Sadiq, M. Heterogeneous photodegradation of industrial dyes: An insight to different mechanisms and rate affecting parameters. *J. Environ. Chem. Eng.* **2020**, *8*, 104364. [[CrossRef](#)]
44. Khan, I.; Saeed, K.; Zekker, I.; Zhang, B.; Hendi, A.H.; Ahmad, A.; Ahmad, S.; Zada, N.; Ahmad, H.; Shah, L.A.; et al. Review on methylene blue: Its properties, uses, toxicity and photodegradation. *Water* **2022**, *14*, 242. [[CrossRef](#)]
45. Afzal, S.; Quan, X.; Zhang, J. High surface area mesoporous nanocast LaMO<sub>3</sub> (M=Mn, Fe) perovskites for efficient catalytic ozonation and an insight into probable catalytic mechanism. *Appl. Catal. B Environ.* **2017**, *206*, 692–703. [[CrossRef](#)]
46. Zhang, J.; Hu, Y.; Jiang, X.; Chen, S.; Meng, S.; Fu, X. Design of a direct Z-scheme photocatalyst: Preparation and characterization of Bi<sub>2</sub>O<sub>3</sub>/g-C<sub>3</sub>N<sub>4</sub> with high visible light activity. *J. Hazard. Mater.* **2014**, *280*, 713–722. [[CrossRef](#)] [[PubMed](#)]
47. Sillanpää, M.; Ncibi, M.C.; Matilainen, A. Advanced oxidation processes for the removal of natural organic matter from drinking water sources: A comprehensive review. *J. Environ. Manag.* **2018**, *208*, 56–76. [[CrossRef](#)] [[PubMed](#)]
48. Sun, W.; Sun, Y.; Zhu, H.; Zheng, H. Catalytic activity and evaluation of Fe-Mn@Bt for ozonizing coal chemical biochemical tail water. *Sep. Purif. Technol.* **2020**, *239*, 116524. [[CrossRef](#)]